Soil Dynamics and Earthquake Engineering 187 (2024) 108898

Contents lists available at ScienceDirect

Soil Dynamics and Earthquake Engineering

journal homepage: www.elsevier.com/locate/soildyn

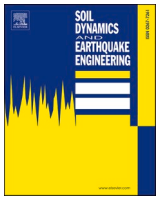

Seismic performance analysis and optimization of a re-centring and self-balanced inerter driven by a rhombic linkage

Liyu Xie [a], Zijian Yang [a], Qiang Xie [a], Yuehui Cao [a], Songtao Xue [a,b,*]

[a] Department of Disaster Mitigation for Structures, Tongji University, Shanghai, China
[b] Department of Architecture, Tohoku Institute of Technology, Sendai, Japan

ARTICLE INFO

Keywords:
Re-centring and self-balanced inerter
Fix-point theory
Nonlinear modelling
Vibration mitigation

ABSTRACT

This paper proposes a re-centring and self-balanced inerter (RSBI). The rhombic linkage achieves self-balanced of the torque on the screw, which releases the constraints demanded at the end of the screw and reduces the working wastage and cost of the screw. The flywheel's re-centring feature is guaranteed by introducing a self-resetting spring and enhances the stability of the system. More specifically, firstly, the resonance analysis method provides the optimized mounting angle of the RSBI's rhombic linkage. Then, the user-friendly optimal design strategy of the four-parameter inerter system, are derived by applying the fixed-point theory, and the validity of the optimized parameters is verified by parameter and time history analysis. Finally, nonlinear model of the RSBI is performed to account for the nonlinearity due to the variation of the rhombic linkage angle at large working strokes. The nonlinear amplitude frequency response function of the system is obtained using the harmonic balance method and the working stroke of the inerter is classified by comparing it with the linear frequency response function. The device proposed in this paper provides a good control effect on the displacement and acceleration control of the main structure under multiple seismic waves. The nonlinearity of the device is appropriately exploited to almost double the working stroke of the inerter, which can effectively reduce the size of the device.

1. Introduction

Unfavourable vibrations such as earthquakes and wind-induced vibration have more and more significant consequences on the safety and comforts of structures as buildings evolve in a higher and more flexible direction, increasing the challenge of structural vibration control [1–3]. Energy dissipation and vibration reduction technologies are commonly used to alleviate this problem in new buildings, as well as to strengthen and restore the existing buildings. Passive control methods that do not require external energy input are the most extensively researched [4,5]. As one of the most prominent vibration control systems, the tuned mass damper (TMD) has significant advantages in peak resonance control [6–9]. However, when the dead load of the structure is large, the additional mass required for the control effect of the TMD is also significant. For instance, at the peak of the Citi Corp Centre in New York, a TMD with an additional mass of approximately 370t has been incorporated, whereas the TMD at the summit of China's tallest building, the Shanghai Centre, weighs 1,000t. And this additional mass is carried entirely by the structure under gravity, adding to handling costs.

Recently, the inerter-based control system proves to be an efficient solution for lightweighting [10–12]. The inerter is a two-terminal mass element whose force is directly proportional to the disparity in acceleration between its two terminals. Based on an analogy between mechanical and electrical networks, Smith [13] first termed this two-terminal inertial element as inerter and proposes a rack and pinion inerter. Depending on the different physical mechanisms, it is possible to achieve an amplification of the apparent mass associated with its inertial force, thus achieving a lightweighting of the required real physical mass. The initial implementation of an inerter on a tangible apparatus can be attributed to Kawamata [14] 's fluid mass pump, which employs the fluid's inertial resistance. In recent years, inerter-based vibration damping systems have emerged as a prominent technology in various fields including automotive suspensions [15], building structures [10,16], bridge cables [17], and spacecraft [18]. As one of the most well-known examples of inerter in civil engineering., Ikago [10,19,20]team presented a complete inerter system called tuned viscous damping system (TVMD). The system consists of a viscous damper, an inerter and a tuned spring, in which the apparent mass amplification of

* Corresponding author. Department of Disaster Mitigation for Structures, Tongji University, Shanghai, China.
E-mail address: xue@tongji.edu.cn (S. Xue).

https://doi.org/10.1016/j.soildyn.2024.108898
Received 23 February 2024; Received in revised form 15 July 2024; Accepted 6 August 2024
Available online 5 September 2024

the inerter is achieved by means of a ball screw. In 2014, Lazar et al. [16,17] also proposed a class of inertia-based damping systems called tuned inertia damper (TID) and verify the superior damping performance of TID by comparing it with conventional viscous dampers. In the same year, based on the application of inerter and the generalization of TMD system Marian et al. [21] proposed the tuned mass damper inerter (TMDI) and verify its better performance under random excitation compared to TMD. Meanwhile, the TVMD, TID and TMDI are the three most widely used topologies for inerter systems in civil engineering [12,17,22,23]. Subsequently, Zhang and Pan et al. [24–26] explored the damping effects of different topological combinations of stiffness elements, damping elements and inertial elements of inerter system, and propose an easy design optimization method from the target damping ratio. Furthermore, they theoretically derived the relationship equation of the damping enhancement of the inerter system, and reveal the working mechanism of the inerter system. In addition to a direct vibration control device, Salah et al. [27]proposed a double mass tuned damper inerter (DMTDI) which consists of two TMDs placed at the roof of the building and connected via an inerter. The inerter backward action is transmitted to the secondary mass instead of the building which enhances the performance of device.

Furthermore, some scholars focus on the physical mechanism of apparent mass amplification of inerter. The most commonly employed methods are ball-screw [10,28], rack-and-pinion [29,30], fluid [31,32], and electromagnetic systems [33,34]. Ball screw type inerter is one of the more mature, which converts the translational motion of the screw into the high-speed rotation of the flywheel to achieve the effect of apparent mass amplification. Arakaki et al. [35,36] originally developed a rotary tube damper using a ball screw mechanism to enhance the energy dissipation capacity of viscous damper. Based on the research of Arakaki et al., Kuroda et al. [37] attached a large mass flywheel to the rotary tube damper and obtain a device dominated by inertial force called a Gyro-mass damper. Hwang et al. [38] proposed a rotary inertia damper for vibration control based on the ball screw amplification mechanism and used toggle brace systems to magnify the deformation of the damper. Subsequently, Ikago et al. [10] proposed the TVMD, a proven vibration damping system based on the mechanism of amplified inertia of ball screws and the introduction of tuned springs. Y Sugimura et al. [39] applied the ball screw type inerter to a real steel building and obtained an apparent mass of 5600t with a real physical mass of 560 Kg.

The main cost of a ball screw inerter is the screw. This is because the quality of the screws is very important to reduce unnecessary nonlinearities such as friction and backlash, and to take up the increased inertial forces due to the increasing apparent mass. Papageorgiou et al. [40] and Wang and Su [41] described the friction and backlash effects of the ball-screw inerter that can occur. These nonlinearities can introduce errors into the original linear modelling assumptions or even be detrimental to the control effect [42,43]. Xie et al. [22,44] has developed a self-balanced inerter that uses screw rod with right-hand and left-hand threads to balance the torque. The imbalanced torque on the screw may result in a deviation in the mounting position of the screw, thereby increasing the working wastage of the screw or even leading to its destruction. The self-balanced inerter also relieves torque constraints at the end of the screw, reducing the requirement for screw support bearings and allowing a purely tensile connection to the inerter system in the form of a cable. The strategy of cable connection is adaptable to the building layout of the structure to be controlled which facilitates the installation of vibration control devices. Nevertheless, the machining of the screw rod with right-hand and left-hand threads further increases the cost of the screw. Therefore, this paper employs symmetric rhombic linkages to drive the inerter system to achieve the self-balanced characteristics without increasing the cost of the screw which also reduce the working wastage of the screw. Previously, Nagarajaiah [45] implemented a new semi-active continuously and independently variable stiffness (SAIVS) device through a plane rhombus configuration and combined it with the TMD to solve the problem of invariant stiffness tuning failure which can lead to degradation of control performance. In addition, in order to maintain the working stroke of the inerter, a self-resetting spring is introduced into the device in parallel with the inerter. Previous studies [46–48] have demonstrated the introduction of negative stiffness springs in the similar position as a substitute, effectively increasing the control frequency band and enhancing the performance of the device. It is noteworthy that the system's stability after incorporating the negative stiffness spring requires discussion. Furthermore, since the device proposed in this paper must limit the working stroke of the inerter, the self-resetting spring must be guaranteed and does not contradict the study of incorporating the negative stiffness device.

This paper explores the vibration reduction performance of a re-centring and self-balanced inerter system, and the main organization of the paper is as follows: Section 2 establishes the mechanical model of the RSBI and the equations of motion for a single-degree-of-freedom structure equipped with the RSBI system, and the optimal angles of the rhombic linkage to be probed under resonance conditions; Section 3 obtains the optimum parameters of the RSBI system that are easily designed by applying fixed-point theory and parameter analysis, and divides the working stroke of the RSBI with nonlinear modelling. Section 4 confirms the effectiveness of the RSBI system under different seismic waves and the possibility of utilizing the nonlinearity. Finally, the paper's main conclusion is presented in Section 5.

2. Theoretical analysis of RSBI

2.1. Mechanical model

Fig. 1 shows a schematic illustration of the RSBI, which includes a screw, two flywheel-nut components, four connecting rods arranged in a rhombus, and two restoring springs. The terminals and rhombic linkage transfer a structure's inter-story drift into deformation of the restoring springs and high-speed rotating motion of the flywheel. Two symmetrical flywheels rotate in opposite directions to balance the torque on the screw. The restoring springs return the device to its original condition

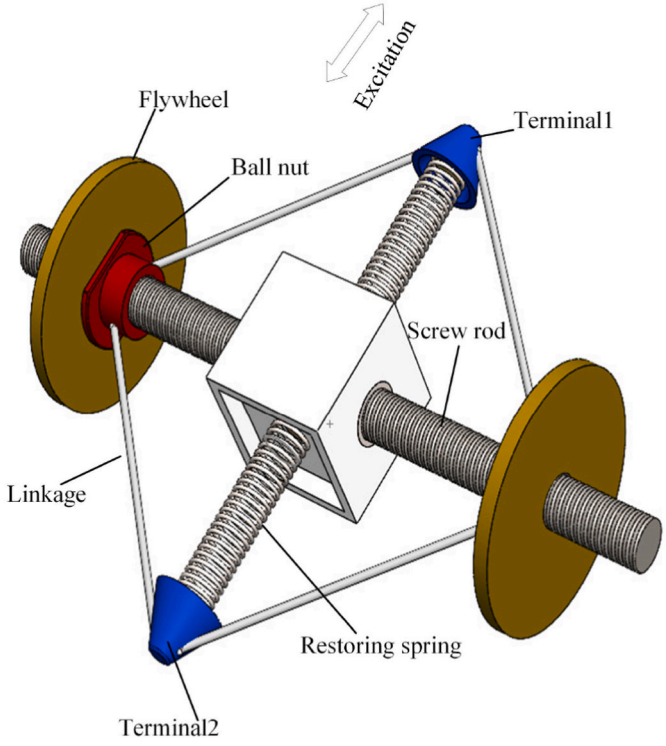

Fig. 1. Schematic representation of the RSBI.

after the excitation.

Fig. 2 illustrates a detailed construction diagram of the RSBI. The lead length and radius of the screw are L_d and r; the mass and the radius of the flywheel are m_b and R; F_T is the output force of the RSBI; α is the inclined angle between the rhombic linkage and restoring spring; the displacement, velocity, and acceleration of the terminal are x, $\dot{x}$ and $\ddot{x}$ respectively; the direction is taken close to the screw as positive; the displacement, velocity, and acceleration of the ball nut are y, $\dot{y}$ and $\ddot{y}$ respectively, the direction is away from the centre of the screw as positive; the rotation angle, angular velocity, and angular acceleration of the flywheel are φ, $\dot{\varphi}$ and $\ddot{\varphi}$, respectively. Under the assumption of a small working stroke, the relationship between RSBI terminal displacement and ball nut displacement is illustrated in Eq (1).

$$x = \frac{y}{\tan\alpha} = \frac{L_d}{2\pi}\frac{\varphi}{\tan\alpha} \tag{1}$$

Considering the stiffness of the restoring spring is k_b, the force in a restoring spring is obtained by:

$$T = k_b x \tag{2}$$

Here, this variable force T always restores the RSBI to the original position, which is the source of the self-centering property. The damping of the device is provided by a viscous damper arranged along the direction of the screw, with an equivalent damping coefficient of c_b, and the overall damping force is:

$$F_c = c_b\dot{y} = c_b\dot{x}\tan\alpha \tag{3}$$

Also, the inertial torque M_i is caused by the moment of inertia of the flywheels and the angular acceleration $\ddot{\varphi}$ as follows:

$$M_i = I\ddot{\varphi} = \frac{m_b}{2}\left(r^2 + R^2\right)\ddot{\varphi} \tag{4}$$

Then the inertial output force can be calculated as follows:

$$F_I = \frac{M_i}{r\tan\theta} = \frac{1}{2}\left(\frac{2\pi}{L_d}\right)^2 \tan\alpha\left(r^2 + R^2\right)m_b\ddot{x} \tag{5}$$

where. Is the tilt angle of the screw, $\tan\theta = L_d/(2\pi r)$.

This paper assumes that the contact between the screw and the flywheel is ideal without considering friction and clearance. This assumption is reasonable given that the non-linearities have less effect when the ball screw is in normal operation. The inertia force generated by the flywheel sliding in the direction of the screw is negligible compared to the inertia force generated by its rotation. Thus, the total force of the RSBI is:

$$F_T = T + (F_c + F_I)\tan\alpha \tag{6}$$

Substituting Eqs (2), (3) and (5) to (6), the total output F_T can be described as:

$$F_T = \frac{1}{2}\left(\frac{2\pi}{L_d}\right)^2 \tan^2\alpha\left(r^2 + R^2\right)m_b\ddot{x} + c_b\dot{x}\tan^2\alpha + k_b x \tag{7}$$

As is shown in Fig. 2b, the moment of equilibrium equation of the screw is:

$$T_L + T_R = J_L\ddot{\varphi} + (-J_L\ddot{\varphi}) = 0 \tag{8}$$

where $J_L = J_R = m_b\left(R^2 + r^2\right)/2$.

Thus, the torque on the screw generated by two symmetrical flywheels rotating in different directions is balanced. And the force F_T can be simplified as:

$$\begin{cases} F_T = m_d\tan^2\alpha\ddot{x} + c_d\tan^2\alpha\dot{x} + k_d x \\ m_d = \frac{1}{2}\left(\frac{2\pi}{L_d}\right)^2\left(r^2 + R^2\right)m_b, c_d = c_b, k_d = k_b, \tan\alpha = \frac{\sqrt{l^2 - (x_0 + x)^2}}{(x_0 + x)} \end{cases} \tag{9}$$

where x_0 is the length of the primary restoring spring and l is the length of the rhombic linkage.

Fig. 3 shows the simplified mechanical model of the RSBI, which consists of an inerter element, a damper element and a restoring spring element, all connected in parallel.

Substituting $F_T = m_d A_g e^{i\omega t}$ and $x = Xe^{i\omega t}$, Eq (9) can be rewritten as:

$$\frac{X}{A_g\omega_d^2} = \frac{1}{1 + 2\xi_d i\beta_d\tan^2\alpha - \beta_d^2\tan^2\alpha} \tag{10}$$

where F_T can be seen as the external excitation on RSBI. The damping ratio and the natural frequency of RSBI can be expressed as $\xi_d = c_d/2m_d\omega_d$, $\omega_d = \sqrt{k_d/m_d}$ and $\beta_d = \omega/\omega_d$.

The displacement amplification factor is obtained as:

$$H_L = \left|\frac{X}{A_g\omega_d^2}\right| = \sqrt{\frac{1}{\left(1 - \beta_d^2\tan^2\alpha\right)^2 + \left(2\xi_d\beta_d\tan^2\alpha\right)^2}} \tag{11}$$

It is a fact that the effective control band of a linear inerter system is

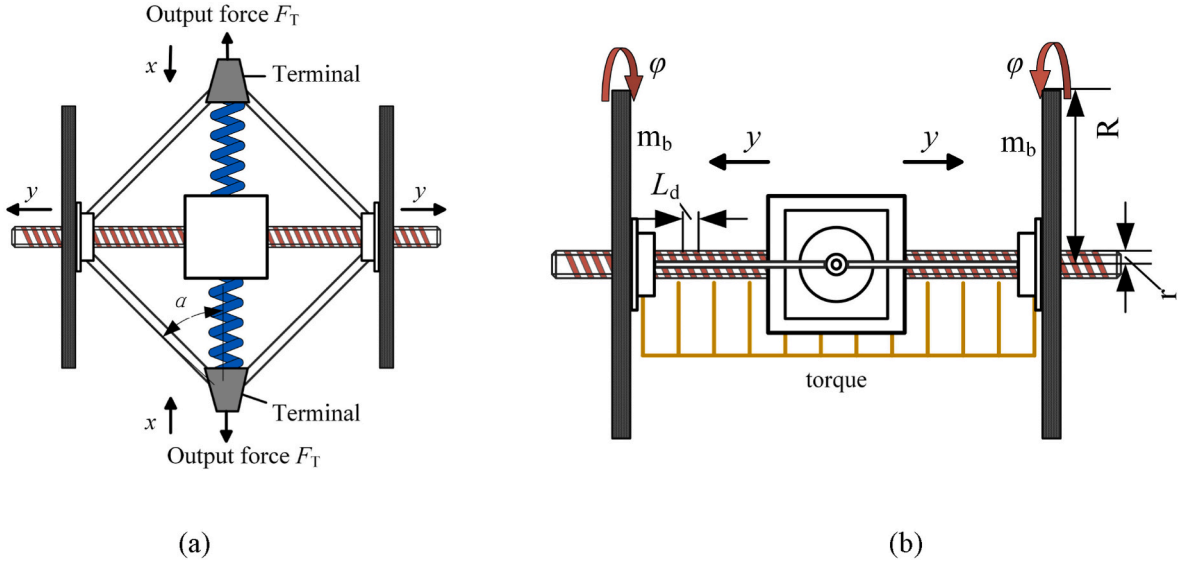

Fig. 2. Detailed diagram of RSBI; (a) Motion Schematic; (b) Torque of the screw.

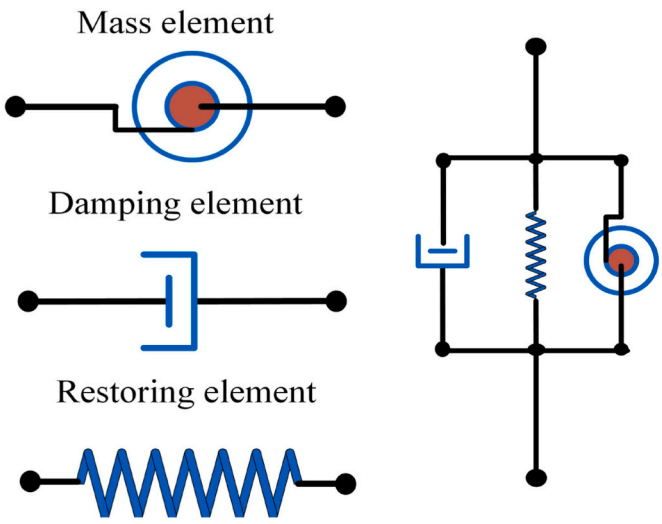

Fig. 3. Mechanical model of the RSBI.

close to its own natural frequency. The inerter system consumes energy most efficiently when the external excitation is near the natural frequency of the system. Fig. 4 illustrates the displacement amplification factor's variation with the connecting rod angle α under different intrinsic damping of RSBI when β_d equals unity. The displacement amplification factor gets the maximum value when α approaches 45°, indicated that the RSBI's deformation amplitude X gets the maximum value while external excitation is constant. At this time, RSBI can fully play to the vibration mitigation effect because the damping element takes full advantage of the energy dissipation. Accordingly, the inclined angle α between the rhombic linkage and restoring spring is taken as 45° for all subsequent discussions within this paper.

2.2. Motion equation

To achieve the tuning effect, an additional spring at one terminal is necessary for RSBI's actual use and this combination is termed the RSBI system. Fig. 5 shows the mechanical model of a single-degree-of-freedom (SDOF) structure equipped with a RBIS system when the structure is subjected to a horizontal excitation. It is worth noting that the inerter system is a two-end connection device. In the case of sdof structures, the RSBI system is connected to the structure at one end and

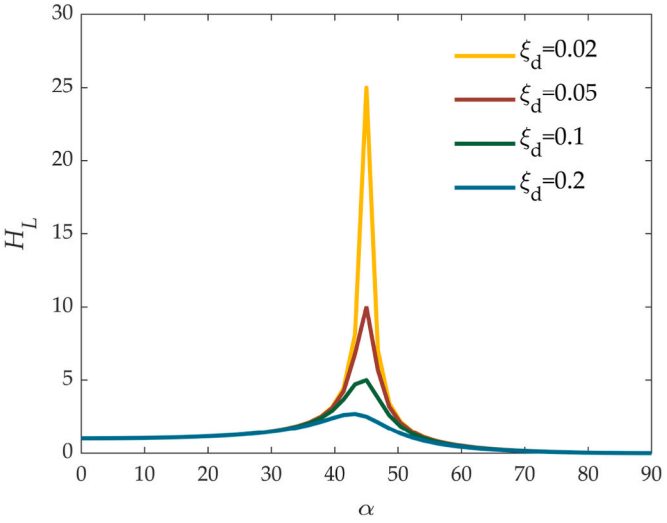

Fig. 4. Displacement amplification factor with $\xi_d = 0.02, 0.05, 0.10$ and 0.20; $\beta_d = 1$.

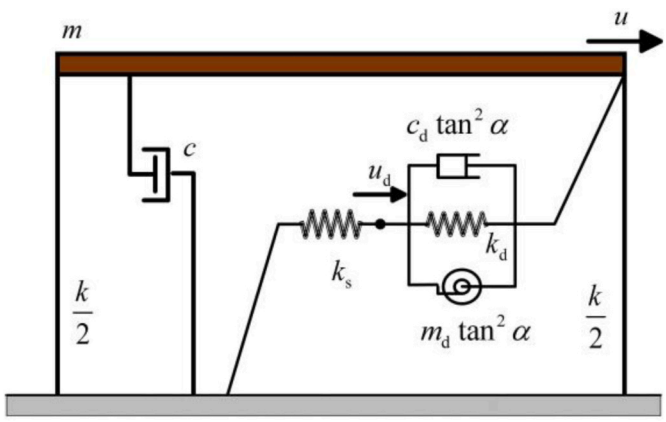

Fig. 5. Mechanical model of a SDOF system with the RSBI system.

grounded at the other end. In the case of multi-degree-of-freedom systems, the system can also be mounted where there is relative displacement within the structure.

As shown, m, c and k are the mass, damping coefficient and stiffness of the primary SDOF system; $m_d \tan^2 \alpha$, $c_d \tan^2 \alpha$ and k_d are the equivalent apparent mass, equivalent damping coefficient and restoring stiffness of the RSBI, and k_s is the stiffness of the tuning spring. The output force of the RSBI is equal to the tuning spring force; u is the main structure displacement and u_d is the displacement of the end of the inerter not connected to the structure.

The governing motion equation can be described as:

$$\begin{cases} m\ddot{u} + c\dot{u} + ku + k_s(u - u_d) = -ma_g \\ m_d\ddot{u}_d \tan^2 \alpha + c_d\dot{u}_d \tan^2 \alpha + k_d u_d = k_s(u - u_d) \end{cases} \tag{12}$$

Based on the previous analysis, it is assumed that the inerter belongs to the small working stroke so that the change of the rhombic linkage angle can be ignored. and specify that $\alpha = 45°$.Then the formula turns into linear as:

$$\begin{cases} m\ddot{u} + c\dot{u} + ku + k_s(u - u_d) = -ma_g \\ m_d\ddot{u}_d + c_d\dot{u}_d + k_d u_d = k_s(u - u_d) \end{cases} \tag{13}$$

Substituting the following expressions, Eq (13) can be rewritten as:

$$\begin{cases} \ddot{u} + 2 \quad \zeta w_s \quad \dot{u} + {w_s}^2 u + \kappa \quad {w_s}^2(u - u_d) = a_g \\ \mu \quad \ddot{u}_d + 2 \quad \xi \quad w_s \quad \dot{u}_d + \chi \quad \kappa \quad ws^2 u_d - \kappa \quad {w_s}^2(u - u_d) = 0 \end{cases} \tag{14}$$

Define the following dimensionless parameters as:

$$\omega_s = \sqrt{\frac{k_d}{m}}, \mu = \frac{m_d}{m}, \zeta = \frac{c}{2m\omega_s}, \xi = \frac{c_d}{2m\omega_s}, \kappa = \frac{k_s}{k}, \chi = \frac{k_d}{k_s} \tag{15}$$

3. Parameter study

3.1. Analysis index

The benefit of employing the inerter system lies in the resonance peak control, so the H_∞ norm criterion is adopted in the control theory. The structural dynamic displacement accurately reflects the magnitude of the dynamic response, whereas the output force of the inerter system efficiently represents the cost of the control system. Hence, both the displacement of the structure and the output force of the inerter system serve as the primary metrics.

Considering the harmonic ground motion is $a_g = A_0 e^{i\omega t}$, substituting $u_0 = U_0 e^{i\omega t}$ and $u_d = U_d e^{i\omega t}$ in Eq (14), the displacement transfer functions H_U, H_{U_d} is obtained as:

$$H_U(i\omega)=\left|\frac{\omega_s^2 U_0}{A_0}\right|=\left|-\frac{2\,i\beta\,\xi-\beta^2\mu+\chi\,\kappa+\kappa}{2\,i\zeta\,\beta^3\mu-2\,i\zeta\,\beta\,\chi\,\kappa+2\,i\beta^3\xi-\beta^4\mu-2\,i\zeta\,\beta\,\kappa-2\,i\beta\,\kappa\,\xi+4\,\zeta\,\beta^2\xi+\beta^2\chi\,\kappa+\beta^2\kappa\,\mu-2\,i\beta\,\xi+\beta^2\kappa+\beta^2\mu-\chi\,\kappa^2-\chi\,\kappa-\kappa}\right| \tag{16}$$

$$H_{U_d}(i\omega)=\left|\frac{\omega_s^2 U_d}{A_0}\right|=\left|-\frac{\kappa}{2\,i\zeta\,\beta^3\mu-2\,i\zeta\,\beta\,\chi\,\kappa+2\,i\beta^3\xi-\beta^4\mu-2\,i\zeta\,\beta\,\kappa-2\,i\beta\,\kappa\,\xi+4\,\zeta\,\beta^2\xi+\beta^2\chi\,\kappa+\beta^2\kappa\,\mu-2\,i\beta\,\xi+\beta^2\kappa+\beta^2\mu-\chi\,\kappa^2-\chi\,\kappa-\kappa}\right| \tag{17}$$

The output force can be described as $F_{\text{out}}=k_s(u_0-u_d)$, the transfer functions H_F is:

$$H_F(i\omega)=\left|\frac{F_{\text{out}}}{mA_0}\right|=\left|-\frac{(2\quad i\beta\quad \xi-\beta^2\mu+\chi\quad \kappa)\kappa\omega_s^2}{2\,i\zeta\,\beta^3\mu-2\,i\zeta\,\beta\,\chi\,\kappa+2\,i\beta^3\xi-\beta^4\mu-2\,i\zeta\,\beta\,\kappa-2\,i\beta\,\kappa\,\xi+4\,\zeta\,\beta^2\xi+\beta^2\chi\,\kappa+\beta^2\kappa\,\mu-2\,i\beta\,\xi+\beta^2\kappa+\beta^2\mu-\chi\,\kappa^2-\chi\,\kappa-\kappa}\right| \tag{18}$$

The maximum displacement response of the structure equipped with an RSBI system and the output force of the RSBI system can be defined as:

$$H_\infty=\max\{H_{U(F)}(i\beta)\} \tag{19}$$

where $\beta=\omega/\omega_s$. Henceforth, the target of vibration control is to minimize the H_∞ norm.

Given the trade-off between the effectiveness of controlling the peak response of structure and the convenience of engineering applications, this paper selects the fixed-point theory [10,49,50] for optimal design. In order to apply the fixed-point theory, it is assumed that the damping ratio ζ of the main structure is 0. Based on Eqs (18) and (19), the displacement amplification factor R_U is defined as follows:

$$R_U=\left|\frac{U_0\omega_s^2}{A_0}\right|=\sqrt{\frac{(\beta^2\mu-\chi\quad \kappa-\kappa)^2+4\quad \beta^2\xi^2}{(-\beta^4\mu+(\chi\quad \kappa+\kappa\quad \mu+\kappa+\mu)\beta^2-\chi\quad \kappa^2-\chi\quad \kappa-\kappa)^2+(2\quad \beta^3\xi+(-2\quad \kappa\quad \xi-2\quad \xi)\beta)^2}} \tag{20}$$

Based on Eq (19) and assumed the inherent damping ratio ζ for the primary structure is 0.05, there are four unknown parameters left, μ,κ,χ and ξ. A series of numerical cases are considered to investigate the effects of parameters, where μ,κ and ξ continuously change in limited parameter space respectively and χ is some specified value. The comparison results were shown in Figs. 6–8 and 9.

As depicted in Fig. 6, the minimum-value regions are located in the upper-right part, showing that a combination of large values of μ and κ is more effective in vibration mitigation, and there exists a preferred value of the parameter when ξ is constant. As shown in Fig. 7, when the mass ratio μ remains constant, a local minimal region also exists inside the contour, which is the ideal region for the parameter to accept its value, since there is less need for the damping ratio. Furthermore, the peak value of the structural displacement response is observed to decrease as the mass ratio μ increases. This finding is consistent with the intuitive notion that a larger mass ratio is associated with a more effective control effect.

Fig. 8 illustrates the distribution of the maximum output force of the inerter system. When the damping ratio ξ is certain, the maximum output force of RSBI system appears in the upper right corner of the contour plot, indicating that larger mass and stiffness ratios correspond to larger output force. As shown in Fig. 9, when the mass ratio is certain, the larger output force appears in the low damping ratio region and is highly sensitive to parameter variation. The local minimal value region of the peak structural displacement in Fig. 7 does not necessarily correspond to a very large force. This indicates that this region may be ideal for parameter values providing a trade-off between control effectiveness and cost.

3.2. Optimal design

Substituting $\xi=0$ and $\xi=\infty$ in Eq (20):

$$|R_U|_{\xi=0}=\left|\frac{\beta^2\mu-\chi\quad \kappa-\kappa}{-\beta^4\mu+(\chi\quad \kappa+\kappa\quad \mu+\kappa+\mu)\beta^2-\chi\quad \kappa^2-\chi\quad \kappa-\kappa}\right| \tag{21}$$

$$|R_U|_{\xi=\infty}=\left|\frac{1}{-\beta^2+1+\kappa}\right| \tag{22}$$

Considering Eqs (21) and (22) are equal at the fixed points and the signs of them, the equation is:

$$\frac{\beta^2\mu-\chi\quad \kappa-\kappa}{-\beta^4\mu+(\chi\quad \kappa+\kappa\quad \mu+\kappa+\mu)\beta^2-\chi\quad \kappa^2-\chi\quad \kappa-\kappa}=\frac{1}{\beta^2-\kappa-1} \tag{23}$$

Rewrite Eq (23) into a quadratic equation about β^2 as:

$$\begin{aligned}&2\quad \beta^4\mu+(-2\quad \chi\quad \kappa-2\quad \kappa+\mu\quad (-\kappa-1)-\kappa\quad \mu-\mu)\beta^2\\&+(-\chi\quad \kappa-\kappa)(-\kappa-1)+\chi\quad \kappa^2+\chi\quad \kappa+\kappa\\&=0\end{aligned} \tag{24}$$

Solving Eq (24) yields the respective frequency ratios at the fixed points on the left and right respectively are β_L and β_R. Combining $|R_U|_{\xi=\infty,\beta=\beta_L}=|R_U|_{\xi=\infty,\beta=\beta_R}$ and the coefficients of β^2 in Eq (24), it can get the relationship that should be satisfied between μ, κ and χ as equations Eq (25).

$$\chi\quad \kappa-\kappa\quad \mu+\kappa-\mu=0 \tag{25}$$

It should be emphasized that the presence of three parameters and only one equation means that there is no way of accessing the specific

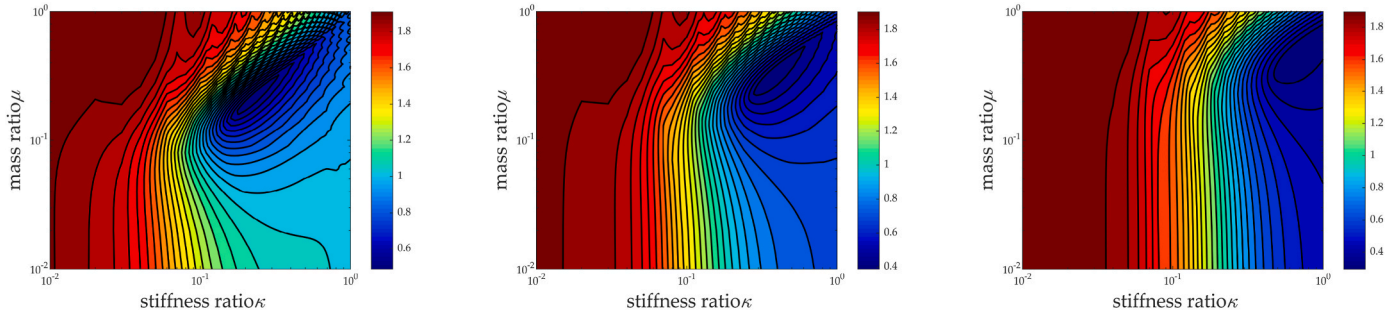

Fig. 6. Contour plots depicting the maximum displacement response of the primary structure for $\mu = [0.01, 1.00]$, $\kappa = [0.01, 1.00]$,$\chi = 0.1$ (a) $\xi = 0.05$; (b) $\xi = 0.10$; (c) $\xi = 0.20$.

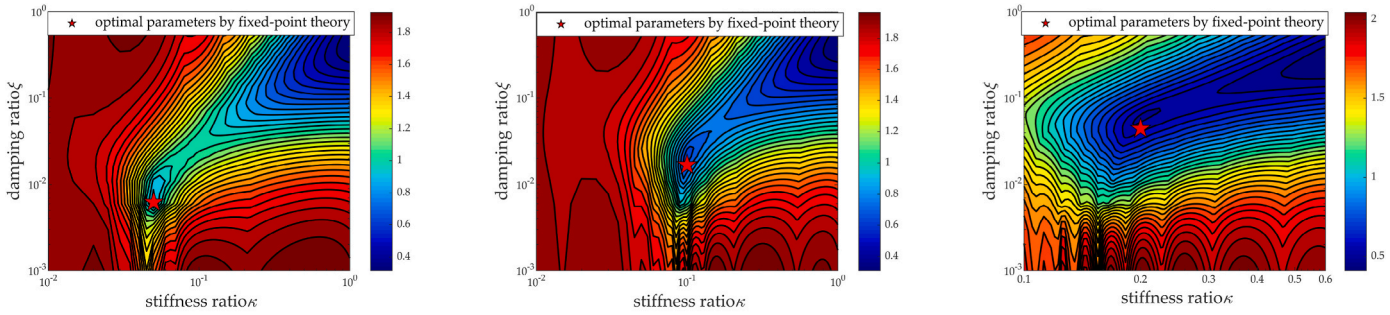

Fig. 7. Contour plots depicting the maximum displacement response of the primary structure for $\xi = [0.01, 1.00]$, $\kappa = [0.01, 1.00]$ (a) $\chi = \mu = 0.05$; (b) $\chi = \mu = 0.10$; (c) $\chi = \mu = 0.20$.

relationship. To aid in design and maintain the use of fixed-point theory while observing Eq (25), the following constraints $\chi = \kappa$ can be imposed artificially. The optimized parameters χ and κ will then take on the values shown in Eq (26).

$$\chi_{\text{opt}} = \kappa_{\text{opt}} = \mu \tag{26}$$

Next, obtain the expression (27) for ξ_{opt} by taking the displacement amplification factor $|R_U|_{\beta=\beta_R}$ a maximum value and substituting Eq (26).

$$\left\{ \xi_{\text{opt}} \middle| f(\mu, \beta_L, \xi_{\text{opt}}) = \frac{\partial R_U}{\partial \beta}\Big|_{\beta=\beta_L} = 0 \right\} \tag{27}$$

In summary, after implementing artificial constraints and employing fixed-point theory, the theoretically optimized values of the simplified four-parameter inerter system are as Eq (28).

Employing the optimization conclusions above, the main structure displacement transfer function image is illustrated in Fig. 10, and it can be observed that the peaks are well constrained at the two fixed points. Moreover, the peak displacement decreases as the mass ratio increases. The mass ratio is also a factor related to the cost of the inerter system, so the appropriate mass ratio can be determined according to the damping requirements. The parameter locations after fixed-point theory optimization are plotted separately in the contours of Fig. 7, and it can be observed that the peak displacements of the structure are all at a locally optimal position. This illustrates that despite the fact that the damping

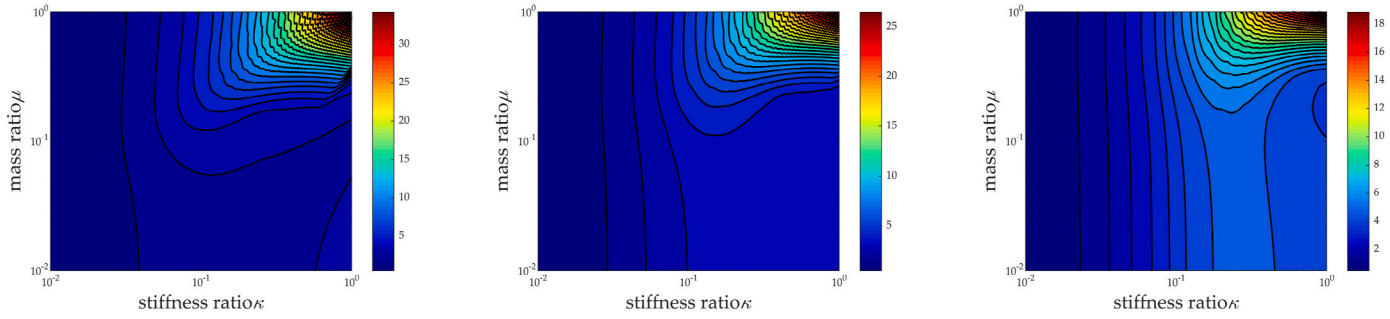

Fig. 8. Contour plots depicting the maximum output force of the inerter system $\mu = [0.01, 1.00]$, $\kappa = [0.01, 1.00]$,$\chi = 0.1$ (a) $\xi = 0.05$; (b) $\xi = 0.10$; (c) $\xi = 0.20$.

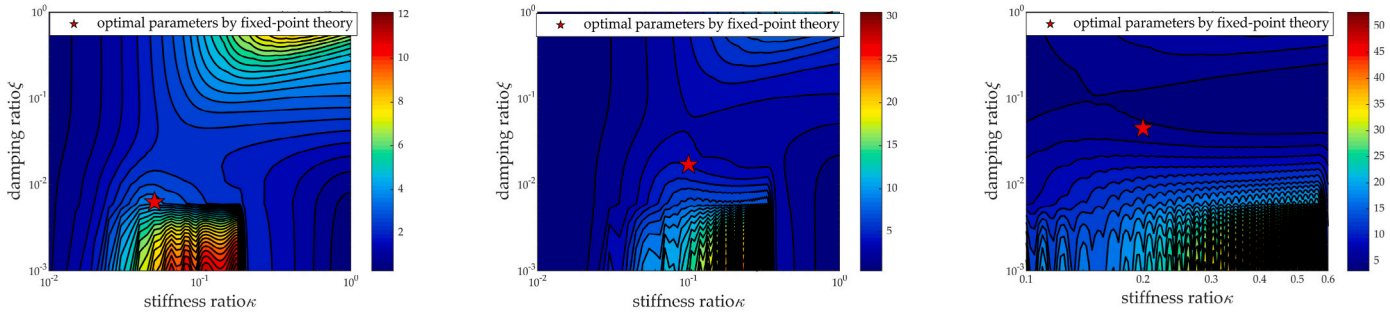

Fig. 9. Contour plots depicting the maximum output force of the inerter system for $\xi = [0.01, 1.00]$, $\kappa = [0.01, 1.00]$ (a) $\chi = \mu = 0.05$; (b) $\chi = \mu = 0.10$; (c) $\chi = \mu = 0.20$.

ratio of the main structure is disregarded by employing the fixed-point theory optimization method, the optimized parameters still offer relatively favorable results. Furthermore, the location of the fixed-point theory optimized parameters is showed in the contour plot of the maximum RSBI output force in Fig. 9, where it is evident that the output force of the device is not significant at this point. This further demonstrates that the parameter optimized by the fixed-point theory in this paper have good results for displacement control and cost control.

$$\begin{cases} \chi_{\text{opt}} = \mu \\ \kappa_{\text{opt}} = \mu \\ \xi_{\text{opt}} = \dfrac{\sqrt{a_1\left(5.7\sqrt{\mu^3}\,\mu^2 + 4\mu^2 + 10\sqrt{a_2} + 5.7\sqrt{\mu^3}\right)\mu^3}}{a_1} \\ a_1 = 2.3\sqrt{\mu^3}\mu^2 + 3.2\mu^3 + 5.7\sqrt{\mu^3}\mu + 3.2\mu^2 + 2.3\sqrt{\mu^3} \\ a_2 = 1.3\,\mu^5 + 1.8\sqrt{\mu^3}\mu^3 + 3.2\,\mu^4 + 1.8\sqrt{\mu^3}\mu^2 + 1.3\mu^3 \end{cases} \tag{28}$$

Next, the effect of the self-resetting stiffness ratio χ on the displacement control of the main structure and the output force of the RSBI system is investigated, assuming that the mass ratio μ of the RSBI system is constant and equal to 0.1. The optimized parameters obtained by varying the imposed artificial constraints, also with the above methodology, are presented in Table 1. As can be observed, with increasing self-resetting stiffness ratio, both the optimally tuned stiffness ratio and the damping ratio decrease. The displacement transfer functions of the primary structure and the output force transfer functions of the RSBI system, corresponding to various optimization parameters are shown in Fig. 11a and b. As the self-resetting stiffness decreases, the maximum structural displacement of the fixed-point decreases, and the maximum output force of the RSBI system decreases. However, since these variations are in a narrow range, it indicates that the control performance of the RSBI system is not sensitive to the self-resetting stiffness. As a result, the subsequent optimized design imposes the limitation that the self-resetting stiffness ratio χ is equivalent to the mass ratio μ.

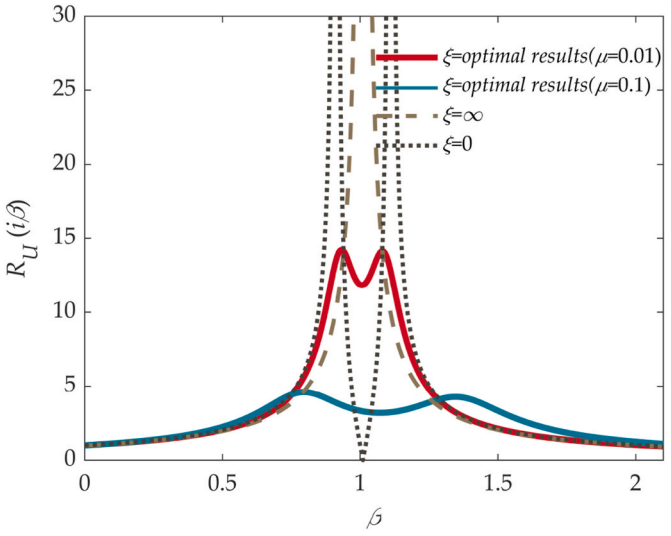

Fig. 10. Displacement transfer function diagram of the primary structure.

3.3. Stroke robustness analysis

Given that the linear modelling approach fails to account for the fluctuation in the rhombic linkage angle, this simplification restricts the actuation stroke of the inerter system. The maximum actuation stroke is pivotal in determining the size of the inerter system. Therefore, nonlinear modelling of the re-centring and self-balanced inerter system is chosen here to take into account the maximum actuation stroke under linear modelling and the control effect after entering nonlinearity.

As depicted in Fig. 2, taking into account the variation in the angle of the rhombic linkage, the inertia force F_{I} and damping force F_{d} of the system are given by following.

$$\begin{cases} F_{\text{I}} = \dfrac{m_{\text{d}}(x_0 + x)}{\sqrt{l_0^2 - (x_0 + x)^2}}\left(\dfrac{(x_0 + x)^2\dot{x}^2}{\left(l_0^2 - (x_0 + x)^2\right)^{3/2}} + \dfrac{\dot{x}^2}{\sqrt{l_0^2 - (x_0 + x)^2}} + \dfrac{(x_0 + x)\ddot{x}}{\sqrt{l_0^2 - (x_0 + x)^2}}\right) \\ F_{\text{d}} = \dfrac{c_{\text{d}}(x_0 + x)^2\dot{x}}{{l_0}^2 - (x_0 + x)^2} \end{cases} \tag{29}$$

It can be observed that the inertial force of the system changes to a non-linear form related to displacement, velocity and acceleration. And the damping force is also in a non-linear form with respect to displacement and velocity. After adopting non-linear modelling, the equations of motion for the single degree of freedom of the equipped inerter system are dimensionless as follows:

$$\begin{cases} \ddot{u} + 2 \quad \zeta w_s \quad \dot{u} + {w_s}^2 u + \kappa \quad {w_s}^2 (u - u_d) = a_g \\ \mu(x_0 + u_d)\left(\dfrac{(x_0 + u_d)^2 {\dot{u}_d}^2}{\left(l_0^2 - (x_0 + u_d)^2\right)^2} + \dfrac{{\dot{u}_d}^2}{l_0^2 - (x_0 + u_d)^2} + \dfrac{(x_0 + u_d)\ddot{u}_d}{l_0^2 - (x_0 + u_d)^2} \right) + 2 \quad \xi \quad w_s \dfrac{(x_0 + u_d)^2}{{l_0}^2 - (x_0 + u_d)^2} \dot{u}_d + \chi \quad \kappa \quad ws^2 u_d - \kappa \quad {w_s}^2 (u - u_d) = 0 \end{cases} \tag{30}$$

The equations of motion contain nonlinear terms for damping and inertial forces. The harmonic balance method and parametric continuation scheme [51,52] is used to solve the amplitude-frequency response function of the system. Fig. 12 shows the process of the parametric continuation scheme used in this paper. Starting from a solution known to the system, an initial guess for the next solution is predicted by the tangent vector and then corrected along a specified arc length to obtain the next solution that satisfies the error accuracy.

Figs. 13 and 14 illustrate the magnitude-frequency response functions of the primary structure for various external excitation amplitudes. The black solid line indicates the displacement frequency response function of the original structure and the red solid line indicates the displacement frequency response function of the structure equipped with the linear RSBI system. The brown dashed lines represent the amplitude-frequency response functions by the Alternating Frequency-Time (AFT) harmonic balance method and parametric continuation scheme. The accuracy of the derivation of the AFT-harmonic balance method is verified by forward and backward sweep analysis. When the amplitude of the external excitation is small, meaning the working stroke of the inerter system falls into the category of small displacements, the nonlinearity is not excited and its amplitude-frequency response function is basically the same as that of the linear model. However, as the external excitation amplitudes increases further, the nonlinear magnitude-frequency response function starts to exhibit differences, specifically the fixed-point theory optimization results in gradual 'tuning failure'. Fig. 15 illustrates the maximum displacement response of the primary structure solved by the harmonic balance method as the damping and stiffness ratios are varied. It can be observed that the contour plot of the maximum displacement does not vary linearly with increasing amplitude of the external excitation. In addition, the amplitude of each order harmonic component of the inerter displacement and velocity-displacement relationship is plotted in Fig. 16 for different external excitation amplitudes. The increase of higher order

Table 1
Optimized values of parameters corresponding to different self-resetting stiffness ratios.

artificial constraints	μ	χ	κ	ξ
$\chi = \mu$	0.1	0.1	0.1	0.017
$\chi = 0.1\mu$	0.1	0.01	0.110	0.018
$\chi = 0.5\mu$	0.1	0.05	0.105	0.018
$\chi = 1.5\mu$	0.1	0.15	0.095	0.016

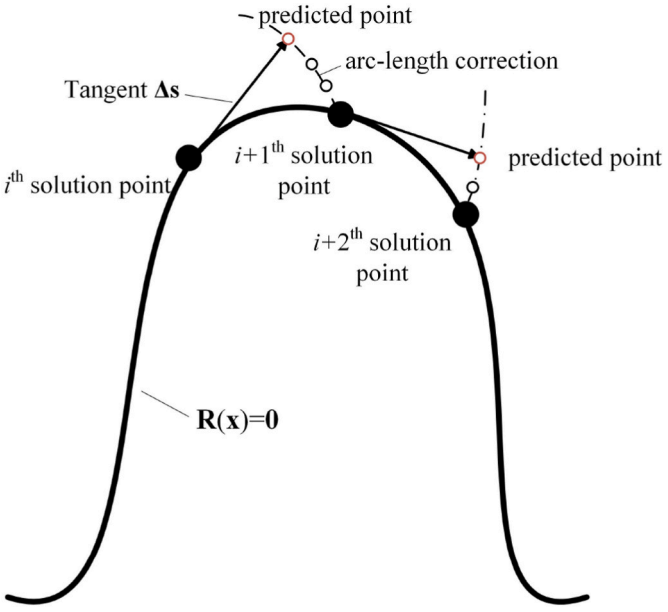

Fig. 12. Schematic diagram of the parametric continuation scheme.

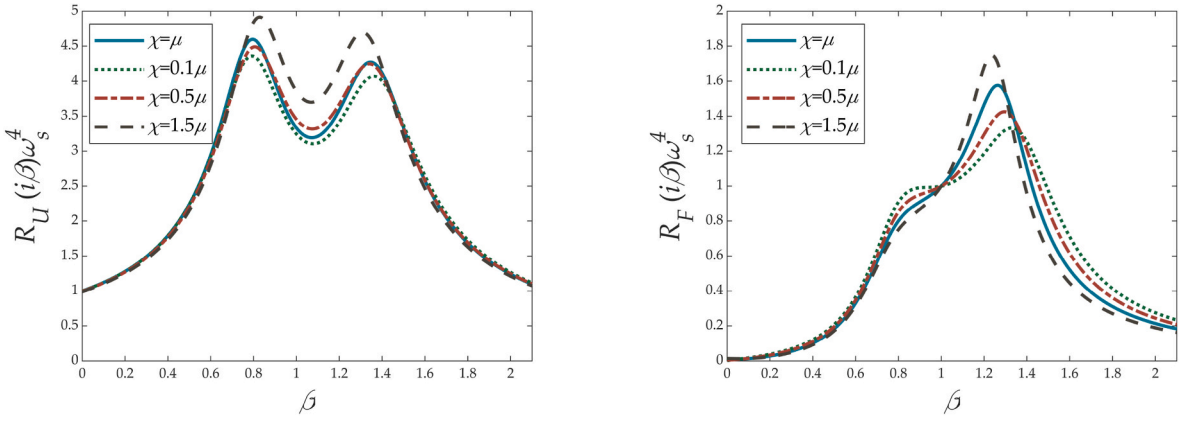

Fig. 11. Diagram of transfer functions corresponding to different self-resetting stiffness ratios (a) Main structural displacement (b) Output force of the RSBI system.

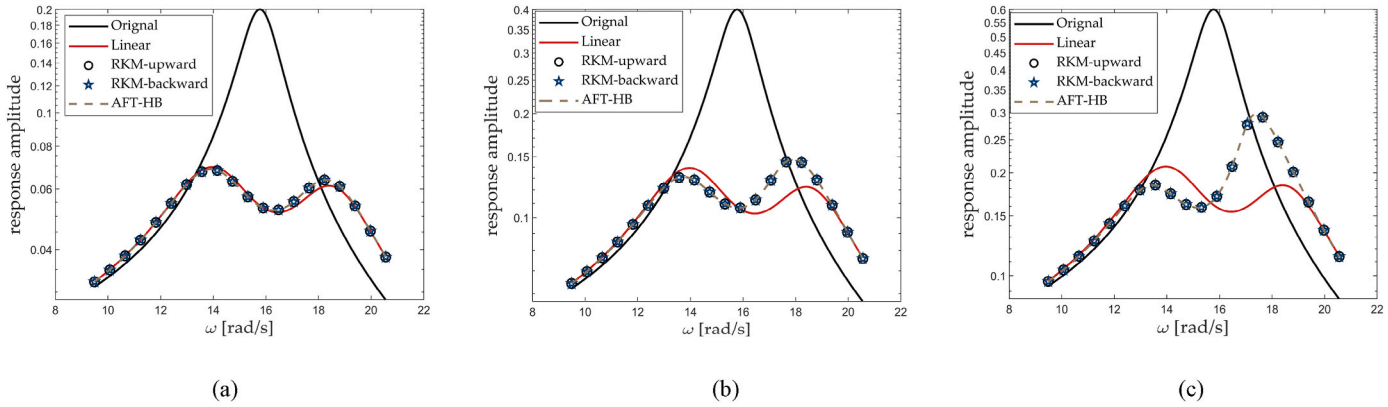

Fig. 13. Displacement response function diagram of the primary structure for $\mu = \chi = \kappa = 0.1$, $\xi = 0.0168$ (a) external excitation amplitude $A_0 = 5$; (b) $A_0 = 10$; (c). $A_0 = 15$.

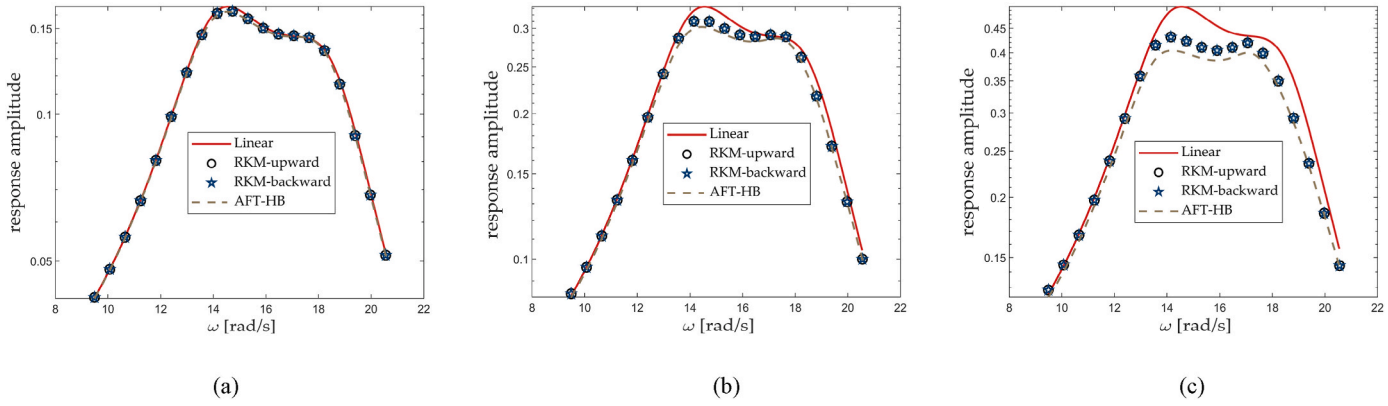

Fig. 14. Displacement response function diagram of the inerter for $\mu = \chi = \kappa = 0.1$, $\xi = 0.0168$ (a) external excitation amplitude $A_0 = 5$; (b) $A_0 = 10$; (c). $A_0 = 15$.

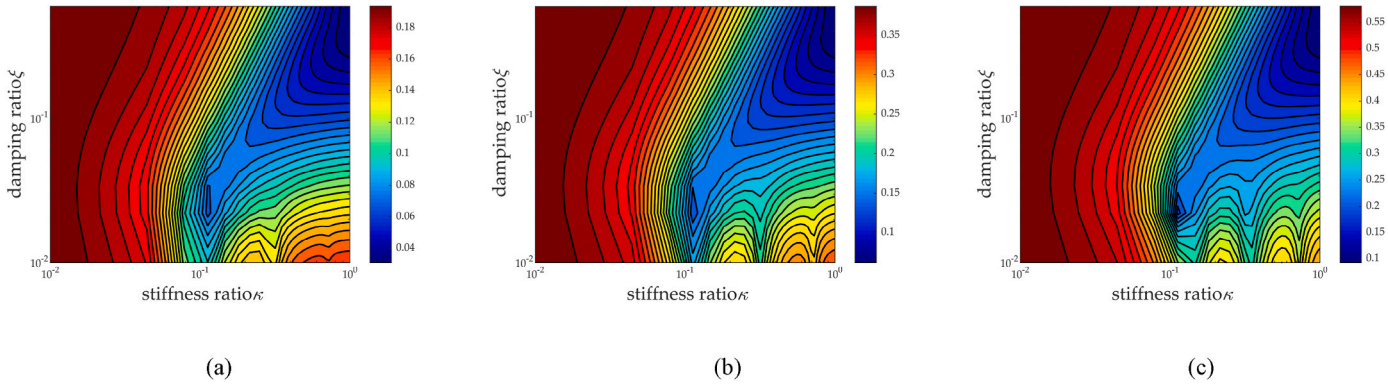

Fig. 15. Contour plots depicting the maximum displacement response of the primary structure for $\chi = \mu = 0.1$, $\xi = [0.01,1.00]$, $\kappa = [0.01,1.00]$ (a)$A_0 = 5$; (b) $A_0 = 10$; (c) $A_0 = 15$.

harmonics in the structural response reveals the nonlinearity. Of the system. This phenomenon detrimentally impacts vibration control of the inerter system.

Using solely the linear range of the inerter system would result in an oversized rhombic linkage and screw, which is not practicable, and the inerter system retains good performance when entering the nonlinear range. Thus, the working stroke of the inerter system is partitioned into a linear range, a nonlinear effective range and a limit range. When the nonlinear amplitude-frequency response function is confined within 10 % above or below the linear displacement transfer function, the working stroke of the inerter system is defined as the linear range. When the peak value of the non-linear amplitude frequency response function is not greater than 40 % of the peak value of the linear displacement transfer function, the working stroke of the inerter system beyond the linear range is defined as the non-linear effective range. In all other cases, the working travel is defined as the limiting range, which means that the maximum working stroke of the inerter system is not recommended to exceed the non-linear effective range. Fig. 17 depicts the division of the stroke of the inerter on the screw. It is evident that the non-linearity of the inerter system can be utilized to almost double the effective working stroke.

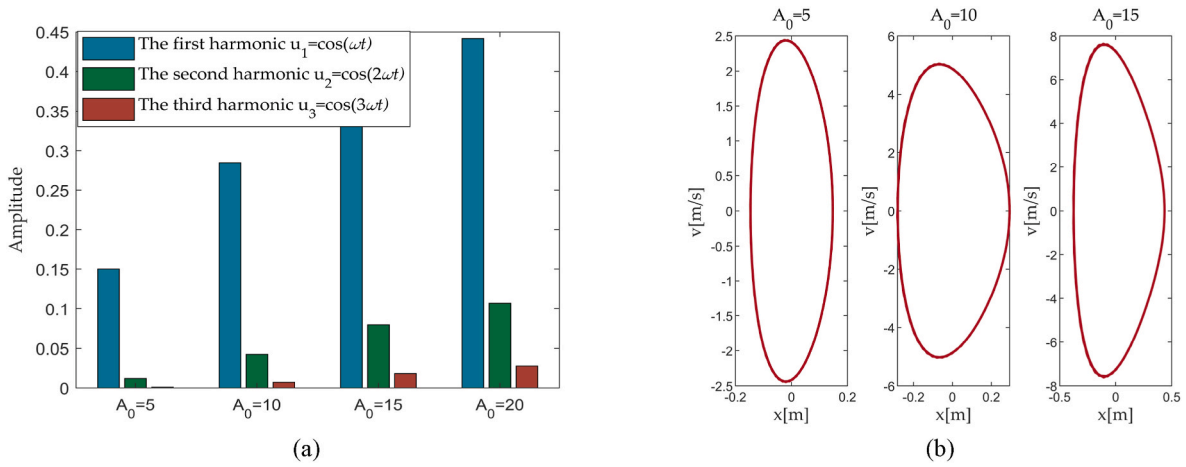

Fig. 16. Motion characteristics under different amplitudes of external excitation (a) histogram of the amplitude of each order harmonic component of the inerter displacement; (b) velocity-displacement diagram of the inerter.

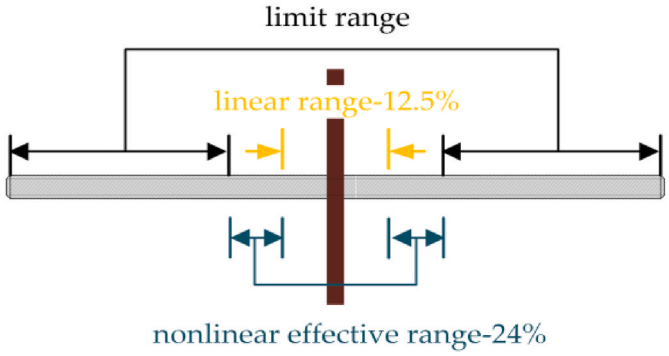

Fig. 17. Diagram of inerter working stroke division.

Table 2
Parameter values for numerical validation.

ω_s (rad/s)	ζ	μ	κ	ξ	χ
3.16	0.05	0.05	0.05	0.0062	0.05

4. Numerical validation for cases

Based on the previously proposed fixed-point theoretical optimization method, the dynamic responses of the original structure, using linear and nonlinear RSBI system equipped structures respectively, are compared under multiple seismic waves which include five natural and two artificial seismic waves as external excitations in accordance with the requirements of the time history analysis of the seismic design code for buildings in China [53]. In order to investigate the performance of linear and nonlinear RSBI, the peak ground acceleration (PGA) of seismic waves in the time history analysis is taken to be 0.22 g and 0.4 g corresponding to different seismic fortification intensities under rare earthquakes according to the seismic design code. The numerical validation assumes that the main structure damping ratio agrees with the concrete structure at 0.05. Considering that the fixed-point theory optimization method used can tune the RSBI system to any frequency, the values of the numerical validation parameters are given in Table 2.

Figs. 18 and 19 illustrate the time history curves of the displacement and acceleration response of the main structure for varying PGAs with El Centro seismic wave inputs. It can be concluded that the optimized RSBI system is effective in the vibration control that the maximum displacement and acceleration responses have significant depressions. Furthermore, when the external excitation amplitude is small (PGA = 0.22 g),

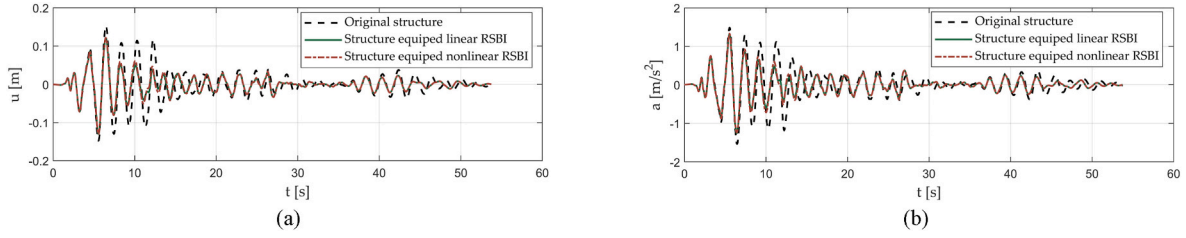

Fig. 18. Example of response of the structure with and without RSBI under El Centro seismic wave PGA = 0.22 g (a) displacement; (b) acceleration.

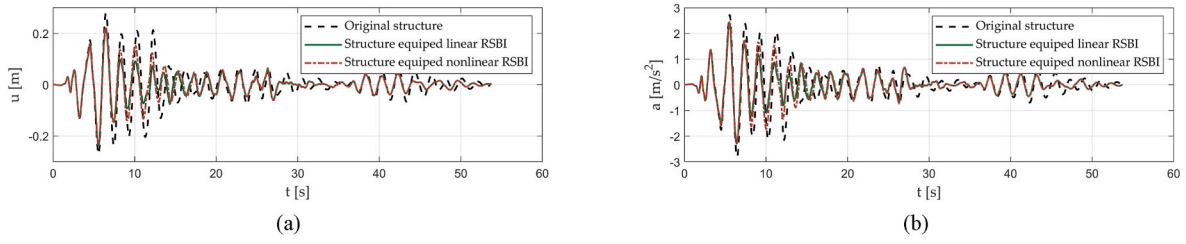

Fig. 19. Example of response of the structure with and without RSBI under El Centro seismic wave PGA = 0.4 g (a) displacement; (b) acceleration.

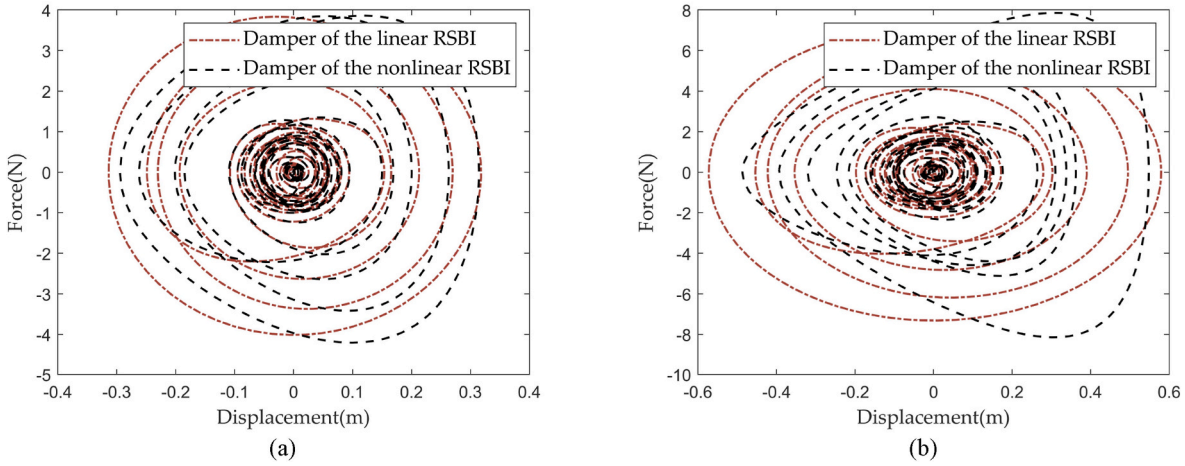

Fig. 20. Comparison of the force-displacement curves of the damper for the linear and nonlinear RSBI. (a) El Centro-PGA = 0.22 g; (b) El Centro-PGA = 0.4 g.

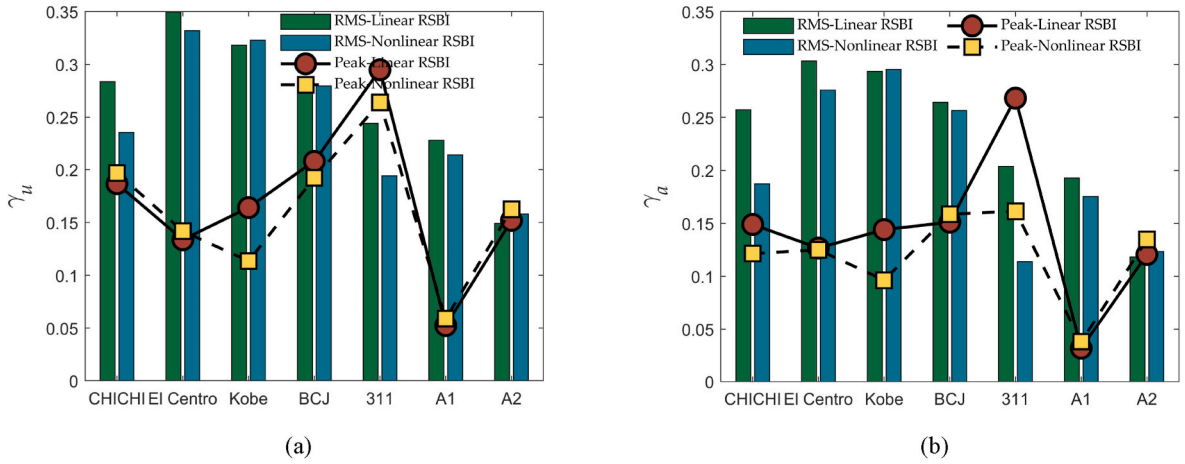

Fig. 21. Diagram of the reduction ratio under multiple seismic waves PGA = 0.22 g (a) displacement; (b) acceleration.

the control effects of linear and nonlinear RSBI are essentially identical, and the damped hysteresis loop shown in Fig. 20a also shows the same energy dissipation capability. And with increasing external excitation amplitude (PGA = 0.40 g) as illustrated in Fig. 20b, a substantial alteration in the shape of the hysteresis loop is evident, suggesting that the nonlinearity of the RSBI is being excited., and the control effect of the linear RSBI is slightly better than that of the nonlinear RSBI.

For a better explanation of the global damping effect under multiple seismic waves, defining the reduction effect γ as:

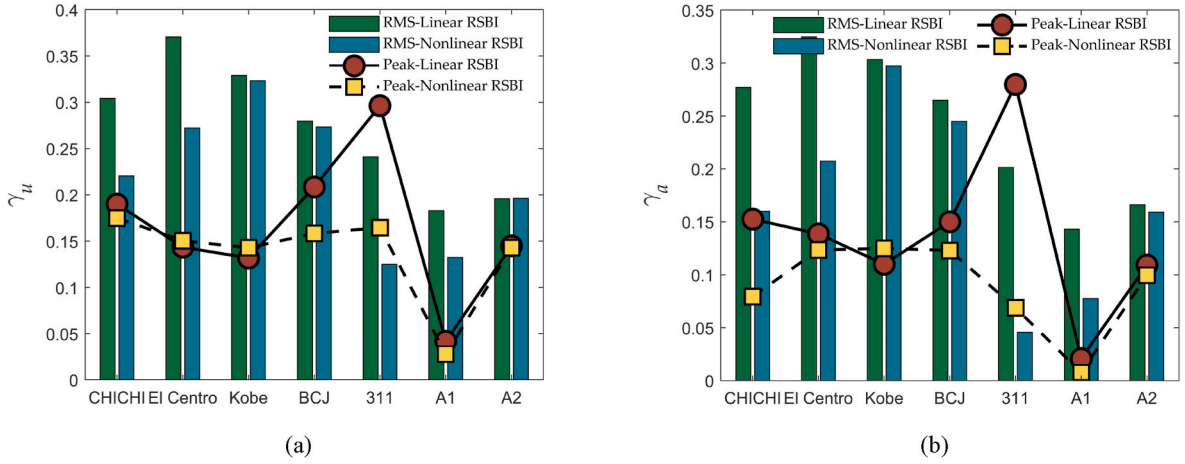

Fig. 22. Diagram of the reduction ratio under multiple seismic waves PGA = 0.4 g (a) displacement; (b) acceleration.

$$\gamma = \frac{\text{Response of unequipped structure} - \text{Response of equipped structure}}{\text{Response of unequipped structure}} \times 100\% \quad (31)$$

Figs. 21 and 22 illustrate the peak and root-mean-square reduction ratios of the structural displacement and acceleration responses under multiple seismic wave inputs. It can be observed that RSBI demonstrates a notable damping effect for different seismic waves. Furthermore, when external excitation amplitude is low, the performance of linear and nonlinear RSBI exhibits minimal discrepancy, with the exception of a few seismic waves. As the excitation amplitude increases, the performance of nonlinear RSBI deteriorates than the linear RSBI, and even becomes significantly worse under individual seismic waves. The study demonstrates that utilizing the linear range of the RSBI provides better damping performance than the nonlinear range. Nevertheless, there exists a tradeoff between efficiency and size, since the working stroke of the inerter is essentially doubled by using the nonlinear range. Therefore, to design the re-centring and self-balanced inerter system, the mass ratio and working stroke of the inerter must be reasonably determined according to the actual situation of the project, such as the installation space of the equipment, the cost and the goal of vibration reduction.

5. Conclusions

With the purpose of reducing the working wastage and cost of the screw and enhancing the practicality of the inerter system, a re-centring and self-balanced inerter system is proposed in this paper. The self-balanced characteristic is achieved by a rhombic linkage driving two symmetrical flywheels that rotate in opposite directions. It is noteworthy that this self-balanced mechanism is achieved in a manner that results in a larger overall size compared to a conventional ball-screw inerter. Through parameter analysis and extension of the application range of the fixed-point theory optimization method, the optimized parameters suitable for engineering design are obtained. Meanwhile, this paper quantifies the working stroke and damping efficiency of the system by comparing the linear and non-linear modelling of the system. The primary findings of this paper are as follows.

1. The self-balanced and re-centring characteristics of the inerter system are achieved by the design of a rhombic linkage and the introduction of a self-resetting spring element. The self-balanced property effectively balances the torque on the screw which decreases machining costs and working wastage. The re-centring property increases the availability and stability of the inerter system during the working life.
2. The application of the fixed-point theory optimization method to a four-parameter inerter system is extended, and the optimized parameter formulations, which are convenient for engineering design, are obtained. The effectiveness of the optimization method is verified through parameter analysis and time history analysis under multiple seismic waves. The proposed device has a good control performance on both the acceleration and displacement response of the structure.
3. Considering the nonlinear properties of the proposed RSBI system, the effectiveness of the device after entering the nonlinear segment is verified by nonlinear modelling. Moreover, by comparing with the amplitude-frequency response function of the linear system, the division of the linear, nonlinear effective and limiting ranges of the working stroke of the device is defined. The nonlinear effective range of the working stroke is appropriately exploited to almost double the working stroke of the inerter, which can effectively reduce the size of the device. The RSBI system's working stroke ought to be designed rationally by incorporating the available equipment space and the vibration damping target in the actual project.

CRediT authorship contribution statement

Liyu Xie: Writing – review & editing, Supervision, Methodology, Investigation, Funding acquisition, Conceptualization. **Zijian Yang:** Writing – review & editing, Writing – original draft, Visualization, Validation, Software, Methodology, Formal analysis, Conceptualization. **Qiang Xie:** Writing – review & editing, Supervision, Methodology, Funding acquisition, Conceptualization. **Yuehui Cao:** Writing – original draft, Visualization, Validation, Software, Methodology, Investigation, Formal analysis, Conceptualization. **Songtao Xue:** Writing – review & editing, Supervision, Methodology, Investigation, Funding acquisition, Conceptualization.

Declaration of competing interest

The authors declare that they have no known competing financial interests or personal relationships that could have appeared to influence the work reported in this paper.

Data availability

Data will be made available on request.

Acknowledgements

The authors would like to acknowledge the support of the National Key R&D Program of China (Grant No.2021YFE0112200) and Natural Science Foundation of Shanghai (Grant 20ZR1461800).

References

[1] Housner G, Bergman LA, Caughey TK, et al. Structural control: past, present, and future. J Eng Mech 1997;123(9):897–971. https://doi.org/10.1061/(ASCE)0733-9399(1997)123:9(897).
[2] Spencer Jr B, Nagarajaiah S. State of the art of structural control. J Struct Eng 2003;129(7):845–56. https://doi.org/10.1061/(ASCE)0733-9445(2003)129:7(845).
[3] Saaed TE, Nikolakopoulos G, Jonasson J-E, et al. A state-of-the-art review of structural control systems. J Vib Control 2015;21(5):919–37. https://doi.org/10.1177/1077546313478294.
[4] Kasai K, Fu Y, Watanabe A. Passive control systems for seismic damage mitigation. J Struct Eng 1998;124(5):501–12. https://doi.org/10.1061/(ASCE)0733-9445(1998)124:5(501).
[5] Marshall JD, Charney FA. Seismic response of steel frame structures with hybrid passive control systems. Earthq Eng Struct Dynam 2012;41(4):715–33. https://doi.org/10.1002/eqe.1153.
[6] Kaynia AM, Veneziano D, Biggs JM. Seismic effectiveness of tuned mass dampers. J Struct Div 1981;107(8):1465–84. https://doi.org/10.1061/JSDEAG.0005760.
[7] Rana R, Soong T. Parametric study and simplified design of tuned mass dampers. Eng Struct 1998;20(3):193–204. https://doi.org/10.1016/s0141-0296(97)00078-3.
[8] Gutierrez Soto M, Adeli H. Tuned mass dampers. Arch Comput Methods Eng 2013;20:419–31. https://doi.org/10.1007/s11831-013-9091-7.
[9] Elias S, Matsagar V. Research developments in vibration control of structures using passive tuned mass dampers. Annu Rev Control 2017;44:129–56. https://doi.org/10.1016/j.arcontrol.2017.09.015.
[10] Ikago K, Saito K, Inoue N. Seismic control of single-degree-of-freedom structure using tuned viscous mass damper. Earthq Eng Struct Dynam 2012;41(3):453–74. https://doi.org/10.1002/eqe.1138.
[11] Marian L, Giaralis A. The tuned mass-damper-inerter for harmonic vibrations suppression, attached mass reduction, and energy harvesting. Smart Struct Syst 2017;19(6):665–78. https://doi.org/10.12989/sss.2017.19.6.665.
[12] Dai J, Xu Z-D, Gai P-P. Tuned mass-damper-inerter control of wind-induced vibration of flexible structures based on inerter location. Eng Struct 2019;199:109585. https://doi.org/10.1016/j.engstruct.2019.109585.
[13] Smith MC. Synthesis of mechanical networks: the inerter. IEEE Trans Automat Control 2002;47(10):1648–62.
[14] Kawamata S. Development of a vibration control system of structures by means of mass pumps [J]. Tokyo, Japan: Institute of Industrial Science, University of Tokyo; 1973.
[15] Hu Y, Chen MZ, Shu Z. Passive vehicle suspensions employing inerters with multiple performance requirements. J Sound Vib 2014;333(8):2212–25. https://doi.org/10.1016/j.jsv.2013.12.016.
[16] Lazar IF, Neild SA, Wagg DJ. Using an inerter-based device for structural vibration suppression. Earthq Eng Struct Dynam 2014;43(8):1129–47. https://doi.org/10.1002/eqe.2390.

[17] Lazar IF, Neild SA, Wagg DJ. Vibration suppression of cables using tuned inerter dampers. Eng Struct 2016;122:62–71. https://doi.org/10.1016/j.engstruct.2016.04.017.
[18] Dong X, Liu Y, Chen MZ. Application of inerter to aircraft landing gear suspension. In: Proceedings of the 2015 34th Chinese control conference (CCC), F. IEEE; 2015 [C].
[19] Ikago K, Saito K, Inoue N. Optimum multi-modal seismic control design of high-rise buildings using tuned viscous mass dampers. In: Proceedings of the proceedings of the 13th international conference on civil, structural and environmental engineering computing stirlingshire. Scotlan, F: Civil Comp Press; 2011 [C].
[20] Ikago K, Sugimura Y, Saito K, et al. Seismic displacement control of multiple-degree-of-freedom structures using tuned viscous mass dampers. In: Proceedings of the Proceedings of the 8th international conference on structural dynamics, EURODYN, F; 2011 [C].
[21] Marian L, Giaralis A. Optimal design of a novel tuned mass-damper–inerter (TMDI) passive vibration control configuration for stochastically support-excited structural systems. Probabilist Eng Mech 2014;38:156–64. https://doi.org/10.1016/j.probengmech.2014.03.007.
[22] Kang J, Xue S, Xie L, et al. Multi-modal seismic control design for multi-storey buildings using cross-layer installed cable-bracing inerter systems: Part 1 theoretical treatment. Soil Dynam Earthq Eng 2023;164:107639. https://doi.org/10.1016/j.soildyn.2022.107639.
[23] Prakash S, Jangid R. Optimum parameters of tuned mass damper-inerter for damped structure under seismic excitation. International Journal of Dynamics and Control 2022;10(5):1322–36. https://doi.org/10.1007/s40435-022-00911-x.
[24] Pan C, Zhang R. Design of structure with inerter system based on stochastic response mitigation ratio. Struct Control Health Monit 2018;25(6):e2169. https://doi.org/10.1002/stc.2169.
[25] Pan C, Zhang R, Luo H, et al. Demand-based optimal design of oscillator with parallel-layout viscous inerter damper. Struct Control Health Monit 2018;25(1):e2051. https://doi.org/10.1002/stc.2051.
[26] Zhang R, Zhao Z, Pan C, et al. Damping enhancement principle of inerter system. Struct Control Health Monit 2020;27(5):e2523. https://doi.org/10.1002/stc.2523.
[27] Djerouni S, Abdeddaim M, Elias S, et al. Optimum double mass tuned damper inerter for control of structure subjected to ground motions. J Build Eng 2021;44:103259. https://doi.org/10.1016/j.jobe.2021.103259.
[28] Smith MC. The inerter: a retrospective. Annual Review of Control, Robotics, and Autonomous Systems 2020;3:361–91. https://doi.org/10.1146/annurev-control-053018-023917.
[29] Saitoh M. On the performance of gyro-mass devices for displacement mitigation in base isolation systems. Struct Control Health Monit 2012;19(2):246–59. https://doi.org/10.1002/stc.419.
[30] Madhamshetty K, Manimala JM. Low-rate characterization of a mechanical inerter. Machines 2018;6(3):32. https://doi.org/10.3390/machines6030032.
[31] Swift S, Smith MC, Glover A, et al. Design and modelling of a fluid inerter. Int J Control 2013;86(11):2035–51. https://doi.org/10.1080/00207179.2013.842263.
[32] Wagg DJ, Pei JS. Modeling a helical fluid inerter system with time-invariant mem-models. Struct Control Health Monit 2020;27(10):e2579. https://doi.org/10.1002/stc.2579.
[33] Gonzalez-Buelga A, Clare LR, Neild SA, et al. An electromagnetic inerter-based vibration suppression device. Smart Mater Struct 2015;24(5):055015. https://doi.org/10.1088/0964-1726/24/5/055015.
[34] Asai T, Araki Y, Ikago K. Energy harvesting potential of tuned inertial mass electromagnetic transducers. Mech Syst Signal Process 2017;84:659–72. https://doi.org/10.1016/j.ymssp.2016.07.048.
[35] Arakaki T, Kuroda H, Arima F, et al. Development of seismic devices applied to ball screw: Part 1 Basic performance test of RD-series. AIJ Journal of Technology and Design 1999;5(8):239–44. https://doi.org/10.3130/aijt.5.239_1.
[36] Arakaki T, Kuroda H, Arima F, et al. Development of seismic devices applied to ball screw: Part 2 Performance test and evaluation of RD-series. AIJ Journal of Technology and Design 1999;5(9):265–70. https://doi.org/10.3130/aijt.5.265.
[37] Kuroda H, Arima F, Baba K, et al. Principles and characteristics of viscous damping devices (gyro-damper), the damping forces which are highly amplified by converting the axial movement to rotary one. Proceedings of the 12th world conference on earthquake engineering. F; 2000 [C].
[38] Hwang J-S, Kim J, Kim Y-M. Rotational inertia dampers with toggle bracing for vibration control of a building structure. Eng Struct 2007;29(6):1201–8. https://doi.org/10.1016/j.engstruct.2006.08.005.
[39] Sugimura Y, Goto W, Tanizawa H, et al. Response control effect of steel building structure using tuned viscous mass damper. Proceedings of the Proceedings of the 15th world conference on earthquake engineering. F; 2012 [C].
[40] Papageorgiou C, Houghton NE, Smith MC. Experimental testing and analysis of inerter devices. https://doi.org/10.1115/1.3023120; 2009.
[41] Wang F-C, Su W-J. Impact of inerter nonlinearities on vehicle suspension control. Veh Syst Dyn 2008;46(7):575–95. https://doi.org/10.1080/00423110701519031.
[42] Wang R, Meng X, Shi D, et al. Design and test of vehicle suspension system with inerters. Proc IME C J Mech Eng Sci 2014;228(15):2684–9. https://doi.org/10.1177/0954406214521793.
[43] Sun X, Chen L, Wang S, et al. Performance investigation of vehicle suspension system with nonlinear ball-screw inerter. Int J Automot Technol 2016;17:399–408. https://doi.org/10.1007/s12239-016-0041-x.
[44] Xie L, Ban X, Xue S, et al. Theoretical study on a cable-bracing inerter system for seismic mitigation. Appl Sci 2019;9(19):4096. https://doi.org/10.3390/app9194096.
[45] Nagarajaiah S. Adaptive passive, semiactive, smart tuned mass dampers: identification and control using empirical mode decomposition. Hilbert transform, and short-term Fourier transform [J]. Structural Control and Health Monitoring: The Official Journal of the International Association for Structural Control and Monitoring and of the European Association for the Control of Structures 2009;16(7–8):800–41. https://doi.org/10.1002/stc.349.
[46] Nagarajaiah S, Chen L, Wang M. Adaptive stiffness structures with dampers: seismic and wind response reduction using passive negative stiffness and inerter systems. J Struct Eng 2022;148(11):04022179. https://doi.org/10.1061/(ASCE)ST.1943-541X.0003472.
[47] Zhao Z, Chen Q, Zhang R, et al. A negative stiffness inerter system (NSIS) for earthquake protection purposes. Smart Structures and Systems, An International Journal 2020;26(4):481–93. https://doi.org/10.12989/sss.2020.26.4.481.
[48] Shen Y, Peng H, Li X, et al. Analytically optimal parameters of dynamic vibration absorber with negative stiffness. Mech Syst Signal Process 2017;85:193–203. https://doi.org/10.1016/j.ymssp.2016.08.018.
[49] Islam NU, Jangid R. Optimum parameters of tuned inerter damper for damped structures. J Sound Vib 2022;537:117218. https://doi.org/10.1016/j.jsv.2022.117218.
[50] Den Hartog JP. Mechanical vibrations [M]. Courier Corporation 1985.
[51] Von Groll G, Ewins DJ. The harmonic balance method with arc-length continuation in rotor/stator contact problems. J Sound Vib 2001;241(2):223–33. https://doi.org/10.1006/jsvi.2000.3298.
[52] Krack M, Gross J. Harmonic balance for nonlinear vibration problems [M]. Springer; 2019.
[53] GB50011–2010, Code for seismic design of buildings. Beijing: China Architecture & Building Press: Ministry of Housing and Urban-Rural Development of the People's Republic of China; 2010.